Mixed-basis cluster expansion for thermodynamics of bcc alloys

Volker Blum and Alex Zunger

National Renewable Energy Laboratory, 1617 Cole Boulevard, Golden, Colorado 80401, USA

To predict the ground-state structures and finite-temperature properties of an alloy, the total energies of many different atomic configurations $\boldsymbol{\sigma} \equiv \{\sigma_i; i=1, \ldots, N\}$, with N sites i occupied by atom A ($\sigma_i = -1$), or B ($\sigma_i = +1$), must be calculated accurately and rapidly. Direct local-density approximation (LDA) calculations provide the required accuracy, but are not practical because they are limited to small cells and only a few of the 2^N possible configurations. The "mixed-basis cluster expansion" (MBCE) method allows to parametrize LDA configurational energetics $E_{LDA}[\sigma_i; i=1, \ldots, N]$ by an analytic functional $E_{MBCE}[\sigma_i; i=1, \ldots, N]$. We extend the method to bcc alloys, describing how to select N_σ ordered structures (for which LDA total energies are calculated explicitly) and N_F pair and multibody interactions, which are fit to the N_σ energies to obtain a deterministic MBCE mapping of LDA. We apply the method to bcc Mo-Ta. This system reveals an unexpectedly rich ground-state line, pitting Mo-rich (100) superlattices against Ta-rich complex structures. Predicted finite-T properties such as order-disorder temperatures, solid-solution short-range order and the random alloy enthalpy of mixing are consistent with experiment.

I. INTRODUCTION

A. The cluster expansion method: Definition and scope

Alloy thermodynamics, including properties at $T=0$, require the knowledge of the excess energy

$$\Delta H_{direct}(\boldsymbol{\sigma}) = E_{tot}(A_{1-x}B_x; \boldsymbol{\sigma}) - (1-x)E_{tot}(A) - xE_{tot}(B), \quad (1)$$

of the solid $A_{1-x}B_x$ relative to the total energy of its constituents A and B. For a given underlying lattice, the degrees of freedom form a configurational vector $\boldsymbol{\sigma}$, whose components $\sigma_i = \pm 1$ record whether a lattice site i is occupied by element A ($\sigma_i = -1$) or B ($\sigma_i = +1$). Since $\Delta H_{direct}(\boldsymbol{\sigma})$ is difficult to calculate quantum mechanically for an exhaustive set of structures $\boldsymbol{\sigma}$, it is often described by way of a cluster expansion (CE) Hamiltonian[1–6]

$$\Delta H_{CE}(\boldsymbol{\sigma}) = J_0 + \sum_i \sigma_i J_i + \sum_{i,j} J_{i,j} \sigma_i \sigma_j + \sum_{i,j,k} J_{i,j,k} \sigma_i \sigma_j \sigma_k + \ldots. \quad (2)$$

$\{J\}$ are the interaction parameters for each pair or many-body combination of lattice sites i, j, k, etc. The cluster expansion[7–10] attempts to describe the energies of all different configurations with the accuracy of present-day density-functional methods. It is based on the fact that Eq. (2) allows to map an arbitrarily complex Hamiltonian with electronic degrees of freedom *exactly* onto a simple sum over crystallographic degrees of freedom.[8] For practical purposes, Eq. (2) is typically recast in terms of symmetry-inequivalent figures.[11] Also, without a loss of generality one may subtract[9] a configuration-dependent reference energy E_{ref} from ΔH. We may expand $\Delta \widetilde{H}_{LDA} = \Delta H_{LDA} - E_{ref}$ as $\Delta \widetilde{H}_{CE}$, so that

$$\Delta \widetilde{H}_{CE}(\boldsymbol{\sigma}) = J_0 + (2x-1)J_1 + \sum_{pairs} J_{pair} D_{pair} \bar{\Pi}_{pair}(\boldsymbol{\sigma})$$
$$+ \sum_{MBs} J_{MB} D_{MB} \bar{\Pi}_{MB}(\boldsymbol{\sigma}). \quad (3)$$

The interaction parameters $\{J_f\}$ now signify all possible inequivalent pairs and many-body (MB) figures f. They are configuration independent,[8] with D_f as each figure's symmetry degeneracy per site—any configuration dependence is contained in the lattice-averaged correlation functions $\bar{\Pi}_f(\boldsymbol{\sigma})$. Although Eqs. (2) and (3) contain, in principle, many interactions, the energetics of bonding is usually determined by relatively short length scales. Therefore, already a finite number of interaction parameters is expected to provide the desired mapping of energetics with sufficient accuracy. The relevant J_f are usually fitted[12] to a number of formation enthalpies calculated by the electronic-structure method to be mapped [local-density approximation (LDA) in our case]. Note that there is no requirement for atoms to remain spatially fixed at the exact positions of a rigid lattice, since the effect of relaxation can be accounted for simply by minimizing ΔH_{LDA} with respect to the unit-cell volume, shape, and internal coordinates for each input $\boldsymbol{\sigma}$. Once numerical values for the parameters of Eq. (3) are available, the payoff is fast access to many quantities of interest. For metallic and semiconductor alloys, these are, e.g., ground-state structures, order-disorder transition temperatures, or short-range order at finite T (see Refs. 13–19 for typical examples), which are directly measurable in experiment.

When constructing a CE for a specific system, the major tasks are to decide (i) what type of figures (pairs, three-body,…) and how many are needed for a given alloy system, and (ii) how to obtain the magnitude of the chosen interactions $\{J\}$ from a well-posed microscopic theory of alloy electronic structure. Over the recent years, $\{J\}$ were often provided by the "mixed-basis cluster expansion"[9,10,20] (MBCE)

$\Delta H_{mix}(AB)$ LRO / T_c	Nb	Ta	Mo
Ta	+5 meV[b] ---		
Mo	−97 meV[a] B2/800K[c]	−114 meV[a] B2/1040K[c]	
W	−30 meV[b] ---	−69 meV[a] B2/920K[c]	+5 meV[b] ---

FIG. 1. Properties of refractory binary alloys from earlier experimental and semiempirical theoretical work: Enthalpies of mixing ΔH_{mix} for the equiatomic composition, predicted long-range order (LRO) and critical temperatures T_c. References: (a) experimental (Refs. 25–27), (b) Colinet *et al.* (Refs. 28 and 29), and (c) Sigli and Sanchez (Ref. 30).

formalism for many fcc-based alloys. In this paper, we describe how to construct a deterministic, LDA-quality MBCE, i.e., how (i) and (ii) are addressed by a systematic assessment of the predictive power of a given CE within a set of input ΔH_{LDA} (cross validation[21,22]), and the iterative enlargement of the LDA input data base as a whole.[10,22] We extend the formalism to a *bcc-based* binary alloy, Mo-Ta. In addition to predicted ground states,[23] we address the system's finite-T thermodynamics (order-disorder transitions, short-range order, and random alloy limit) in relation to experimental work.[24,25]

B. Why Mo-Ta

The most prominent group of fully bcc-based binary alloys (no known phases based on a different type of underlying lattice, e.g., fcc) is formed from the refractory elements Nb, Ta, Mo, and W, located in groups VA and VIA of the periodic system of elements. Figure 1 summarizes some of their pertinent properties.[25–30] The atomic size mismatch of all six possible binary alloys formed between them is below 5%. Their experimental phase diagrams show only continuous bcc (A2) solid solutions,[31] so it is not known if at lower T these form any long-range ordered compounds, or phase separate. Regarding *short*-range order in the solid solution, the only available experimental report pertains to Mo-Ta,[24] where x-ray diffuse scattering showed clear (100)-centric intensity for 21% and 37% Ta. For Mo-Nb,[26] Mo-Ta,[25] and Ta-W,[27] negative enthalpies of mixing were observed, with Mo-Ta giving the most negative value [$\Delta H_{exp}(AB)$ = −114 meV]. No experimental results are available for the remaining combinations, but a number of earlier semiempirical tight-binding-based calculations exist.[28–30] These sources agree upon a clearly less negative ΔH for Nb-W, and even slightly positive values for the in-group combinations Nb-Ta and Mo-W.

Where available, Fig. 1 also contains theoretical predictions regarding long-range order. Focusing on the two shortest pair interactions, the theoretical model of Sigli and Sanchez[30] predicted stable B2 order for Mo-Nb, Mo-Ta, and

Ta-W. A more recent theoretical assessment of Ta-W,[32] also using two pair interactions for thermodynamics, corroborates this finding and suggests an additional D0$_3$-type ground state TaW$_3$ at very low T. The comparison of predicted A2-B2 transition temperatures finds Mo-Ta in the lead again, with a supposed T_c just above 1000 K.

We select Mo-Ta for this study since it shows the largest magnitude of ΔH_{mix} and the highest predicted T_c of the above refractories, and because short-range order of Mo-Ta was already experimentally observed.

II. SHORT-RANGE REAL-SPACE CLUSTER-EXPANSION FOR MO-TA

To use Eq. (3), one must extract the relevant interactions and their numerical values for a particular alloy. To illustrate this, we first examine a short-range cluster expansion in real space: one whose input structures and figures are user-selected based on intuition alone.[12]

Many CE-based works[12,33–40] consider only a set of the spatially smallest J_f, which are then combined with a similar number of "usual suspect" ordered input configurations. Consider the Connolly-Williams method[12] on the fcc lattice: It employed the five shortest figures, obtained from five structural energies—a fully determined fit. Here, we pursue a bcc equivalent of this approach (Fig. 2). We use the $N_F=6$ simplest figures, those with a maximum intracluster distance up to second nearest neighbors: the empty and point interactions, the two smallest pairs, and the smallest triangle and tetrahedron. They are fit to $N_\sigma=6$ ΔH_{LDA} values for elemental A and B, the D0$_3$ structures A$_3$B and AB$_3$, and the B2 and B32 structure.

Figure 3(a) shows the resulting interactions of this approach for Mo-Ta: The dominant term is the nearest-neighbor interaction, with higher interactions of considerably smaller magnitude. In fact, the second nearest-neighbor pair is so much weaker than the first that a casual observer might already claim "convergence." We now use these interactions to predict from Eq. (3) ΔH_{CE} for the 3 000 000 bcc-based crystal structures with up to 20 atoms per unit cell, as given by the exhaustive structure enumeration scheme of Ref. 13. The results are plotted versus composition in Fig. 3(b), where one can identify the predicted ground states as the breaking points of the convex hull encompassing all structures. Convexity is needed because any identified ground state $\boldsymbol{\sigma}_i$ of composition x_i must be lower in formation enthalpy than a phase-separated combination of the closest neighboring ground states $\boldsymbol{\sigma}_{i-1}$ and $\boldsymbol{\sigma}_{i+1}$. We call the difference between these cases the "energetic depth of a ground state," Δ_i,

$$\Delta_i = \Delta H(\boldsymbol{\sigma}_i) - \left[\frac{x_{i+1}-x_i}{x_{i+1}-x_{i-1}}\Delta H(\boldsymbol{\sigma}_{i-1}) + \frac{x_i-x_{i-1}}{x_{i+1}-x_{i-1}}\Delta H(\boldsymbol{\sigma}_{i+1}) \right],$$ (4)

and demand $\Delta_i < 0$. Indeed, this short-range CE exhibits only two ground states: B2 (MoTa), and D0$_3$ (Mo$_3$Ta). Both were also LDA input structures, and one might again conclude "convergence" of the CE from the consistency of the ground-state line and the LDA input set.
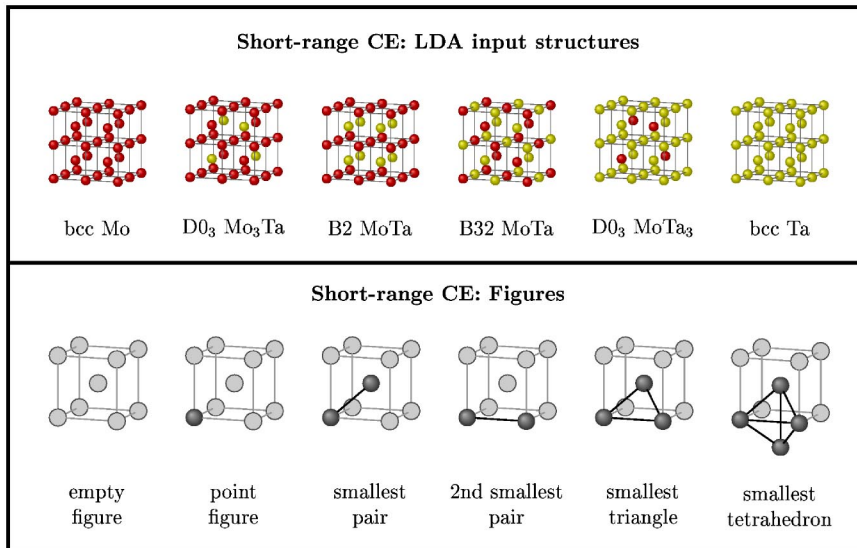
FIG. 2. (Color online) Input structures and figures for the short-range real-space CE of Mo-Ta.

The pitfall of using a small number of intuitively selected structures and figures is the resulting lack of predictive power. This can be assessed by comparing its results with a fully converged cluster expansion of Mo-Ta, described in Sec. VI, which is based on 56 input structures. The important failures of the short-range CE are: (1) Its prediction errors
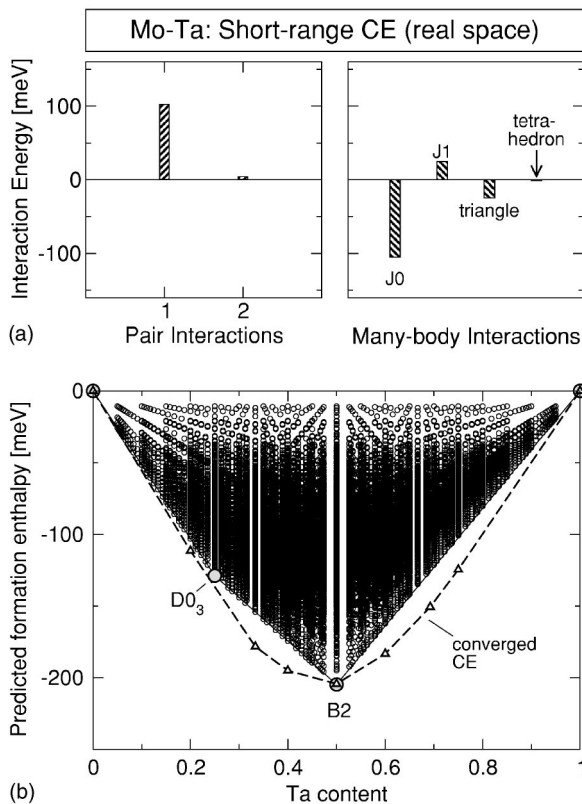

FIG. 3. (a) Symmetry-weighted interactions $D_f J_f$ extracted from the short-range cluster expansion. (b) Exhaustive ground state search (three million structures) based on the short-range cluster interactions. The ground-state line of the converged cluster expansion of Sec. VI (broken line and triangles) is included for comparison.

$\Delta H_{\mathrm{LDA}} - \Delta H_{\mathrm{CE}}$ are much larger than typical intrinsic LDA errors. For instance, the short-range CE is off by 31 meV (17% of ΔH_{LDA}), 31 meV (20%), and 44 meV (30%) for the three structures $C11_b(Mo_2Ta)$, $C11_b(MoTa_2)$, and $B11(MoTa)$, respectively. (2) The ground-state line of the short-range CE is quantitatively far from the converged CE [see Fig. 3(b)], by up to 24 meV. Furthermore, the short-range CE misses all but the B2 ground state (missed six). (3) As pointed out by Laks et al.,[20] the limiting ΔH_{CE} of both elements phase separated on the same coherent lattice is wrong. In a short-range CE, the predicted ΔH_{CE} of $A_m B_n$ superlattices must converge to zero with growing period. However, simple elasticity theory shows that ΔH_f, in fact, remains finite even for the fully phase-separated configuration, since both constituent element crystals must fit the same coherent underlying lattice. Even worse, the limiting ΔH_f may depend on superlattice orientation $\hat{k}$— this is known as the "$k \to 0$ singularity."

In principle, there are several reasons for the qualitative failures (1)–(3): (i) *No information on coherency strain in the infinite superlattice limit is included*. The short-range CE is strictly finite ranged and therefore cannot capture the $k \to 0$ singularity. (ii) *Unphysically few figures*. Since the number of figures is limited by the number of input structures, the "cutoff" of relevant figures is mandated by fit technicalities rather than their physical decay with distance. (iii) *Limited information on atomic relaxation*. The short-range CE is based on high-symmetry ordered structures, which are prohibited by symmetry to relax, both with respect to unit-cell shape and internal coordinates. (iv) *No measure of predictive power*. The short-range CE lacks a quantitative criterion to assess the predictive power of its fitted interactions. (v) *No mechanism to extract relevant input structures and figures*. The short-range CE does not ensure either the suitability of its figure set to describe the material in question, or of its input structures to sample the configuration space optimally for a given material. As a consequence of (i)–(v), a short-range CE approach may yield deceptively "converged" results with respect to ground states and interactions, but as we see, any coincidence with truly converged results is acciden-

tal. While an intuition-based approach which already includes other "usual suspect" structures such as $C11_b$ would potentially come closer to the truth, (i)–(v) will nevertheless remain as qualitative issues. We will next discuss the conceived cure to problems (i)–(v).

III. THE MIXED-BASIS CLUSTER EXPANSION METHOD: PREVIOUS IDEAS TO OVERCOME DIFFICULTIES (I)–(V)

A. Correcting for coherency strain in the superlattice limit

We correct the "$k \to 0$" singularity of the long-period superlattice limit as described in Refs. 10, 20, and 41. We set E_{ref} of Eq. (3) equal to the "constituent strain energy" for finite-ranged configurations

$$E_{\text{ref}}(\boldsymbol{\sigma}) = \sum_{\boldsymbol{k}} \frac{\Delta E_{\text{CS}}^{\text{eq}}(x, \hat{k})}{4x(1-x)} |S(\boldsymbol{k}, \boldsymbol{\sigma})|^2 F(\boldsymbol{k}). \quad (5)$$

Here, S is the structure factor of configuration $\boldsymbol{\sigma}$ (the lattice Fourier transform of $\boldsymbol{\sigma}$), and F a $|\boldsymbol{k}|$-dependent damping factor ($F=1$ in the present work).[41]

$\Delta E_{\text{CS}}^{\text{eq}}(x, \hat{k})$ is defined as the energy limit of an infinite phase-separated alloy (superlattice) on the same coherent underlying lattice, with interface orientation $\hat{k}$:

$$\Delta E_{\text{CS}}^{\text{eq}}(x, \hat{k}) = \min_{a_{\text{in-plane}}, (c/a)_A, (c/a)_B} \{(1-x)\Delta E_A[a_{\text{in-plane}}, (c/a)_A] + x\Delta E_B[a_{\text{in-plane}}, (c/a)_B]\}. \quad (6)$$

B. Use of an unrestricted set of pair interaction figures

Reference 20 also outlines how to include an (in principle) unlimited number of pair interactions by way of a constrained fit approach. This procedure defines the types of parameters to be extracted by the "deterministic MBCE" approach described later in this work. Consider a straightforward fit of N_F pair and many-body figures to N_σ previously calculated LDA input formation enthalpies $\{\Delta H_{\text{LDA}}(\boldsymbol{\sigma})\}$. The CE must then be truncated to $N_F \leqslant N_\sigma$ interactions, since the usual least-squares sum

$$s_{\text{lsq}} = \sum_{\sigma} w_\sigma |\Delta \tilde{H}_{\text{LDA}}(\boldsymbol{\sigma}) - \Delta \tilde{H}_{\text{CE}}(\boldsymbol{\sigma})|^2 \quad (7)$$

(with possibly different fit weights w_σ for each configuration) does not allow for more parameters. So, longer-ranged figures are forced abruptly to zero, regardless of their actual physical value. As a remedy for pairs, one formally includes all pair terms, but amends s_{lsq} with an additional constraint per pair. We minimize

$$s_{\text{MBCE}} = s_{\text{lsq}} + \frac{t}{\alpha} \sum_{\text{pairs}} R_{\text{pair}}^\lambda D_{\text{pair}} J_{\text{pair}}^2, \quad \alpha = \left(\sum_{\text{pairs}} \sqrt{\frac{R_{\text{pair}}^\lambda}{D_{\text{pair}}}}\right)^2. \quad (8)$$

The pairs sum is now only mathematically limited to a maximum n_{pairs}. t is a Lagrangian multiplier and α is a normalization factor. The proper spatial decay of J_{pair} with growing

pair separation R_{pair} is enforced by weight factors R_{pair}^λ.

Using this definition, the individual pair interactions J_{pair} have been replaced as user-adjustable degrees of freedom by t, λ, and the cutoff pair number n_{pairs}. In contrast, the selected multisite interactions $\{J_{\text{MB}}\}$ remain direct degrees of freedom of the MBCE.

C. Description of alloy atomic relaxation

Atomic relaxation in alloys[9,20,42,43] includes (a) *homogeneous* volume deformations δV, (b) relaxation of *cell-external* coordinates $\{a_1, a_2, a_3\}$ [e.g., (c/a) ratio in tetragonal compounds], and (c) relaxation of *cell-internal* atomic positions $\{\mathbf{R}_{\text{int}}\}$. Whereas (a) exists in all configurations, the effects of (b) and (c) depend on the type of configuration considered: High-symmetry structures such as the cubic B2, B32, or $D0_3$ compounds are prohibited by symmetry from having any cell-external or -internal relaxation. Tetragonal structures [such as the AB superlattice of bcc (110) planes, A_1] can have important cell-external (c/a) relaxation, whereas structures that possess a large number of degrees of freedom not fixed by space group symmetry have significant cell-internal relaxation contributions (for instance, changes in interlayer spacing of long-period coherent superlattices $A_m B_n$, which lead to a net shift of the interface between A and B within the cell).

The "relaxation energy" is the difference between relaxed and unrelaxed total energies. In the MBCE with a finite set of figures, relaxation energy includes a piece due to explicit figures $\{J\}$ and the constituent strain, Eq. (5). The first part can be written by inverting Eq. (3),

$$J_f = \sum_{\sigma} \bar{\Pi}_f^{-1}(\boldsymbol{\sigma}) \Delta \tilde{H}_{\text{CE}}(\boldsymbol{\sigma}). \quad (9)$$

$[\bar{\Pi}_f^{-1}(\boldsymbol{\sigma})$ here denotes the inverse of the *matrix* $\bar{\Pi}_f(\boldsymbol{\sigma})$.] This can be reinserted into Eq. (3), yielding

$$\Delta H_{\text{CE}}(\boldsymbol{\sigma}') = \sum_{\sigma} Q_{\sigma', \sigma} \Delta \tilde{H}_{\text{CE}}(\boldsymbol{\sigma}) + E_{\text{CS}}(\boldsymbol{\sigma}'), \quad (10)$$

where $Q_{\sigma', \sigma} = \sum_f \bar{\Pi}_f(\boldsymbol{\sigma}') \bar{\Pi}_f^{-1}(\boldsymbol{\sigma})$. For the random alloy limit at composition x, we take the configurational average over all configurations $\boldsymbol{\sigma}'$ of composition x, $\langle \Delta H_{\text{CE}}(\boldsymbol{\sigma}') \rangle_{\sigma', x}$. Since $\langle \bar{\Pi}_f(\boldsymbol{\sigma}') \rangle_{\sigma', x} = (2x-1)^{l_f}$ for a figure f with l_f vertices, we see that each input structure $\boldsymbol{\sigma}$ enters $\Delta H_{\text{rand}}(x)$ with a well-defined weight

$$\Delta H_{\text{rand}}(x) = \sum_{\sigma} Q_{\text{rand}}(\boldsymbol{\sigma}) \Delta \tilde{H}_{\text{CE}}(\boldsymbol{\sigma}) + \langle E_{\text{CS}}(\boldsymbol{\sigma}') \rangle_{\sigma', x} \quad (11)$$

with

$$Q_{\text{rand}}(\boldsymbol{\sigma}) = \sum_f (2x-1)^{l_f} \bar{\Pi}_f^{-1}(\boldsymbol{\sigma}).$$

We may apply the same approach to formally expand the relaxation contribution of an ordered configuration. The conventional relaxation energy, without separating out constituent strain, is

$$\delta E_{\mathrm{ord}}^{\mathrm{rel}}(\boldsymbol{\sigma}') = \sum_{\sigma} Q_{\sigma',\sigma}[\Delta H_{\mathrm{CE}}^{\mathrm{rel}}(\boldsymbol{\sigma}) - \Delta H_{\mathrm{CE}}^{\mathrm{unrel}}(\boldsymbol{\sigma})]. \quad (12)$$

So, the relaxation energy of the random alloy is a weighted superposition of relaxation energies of ordered compounds

$$\delta E_{\mathrm{rand}}^{\mathrm{rel}}(x) = \sum_{\sigma} Q_{\mathrm{rand}}(\boldsymbol{\sigma})[\Delta H_{\mathrm{CE}}^{\mathrm{rel}}(\boldsymbol{\sigma}) - \Delta H_{\mathrm{CE}}^{\mathrm{unrel}}(\boldsymbol{\sigma})]. \quad (13)$$

Constituent strain is implicit in this equation as a piece due to long-range relaxation, and would appear as an additional term in the actual MBCE formalism.

Recently, Ruban *et al.*[44] proposed a simplified theory of relaxation for the random alloy alone, based on breaking down each configuration into the smallest possible tetrahedra that allow for a space-filling tiling of the alloy ("effective tetrahedron model," ETM). Their approximation for $\delta E_{\mathrm{rand}}^{\mathrm{rel}}$ consists of three steps: First, $\delta E_{\mathrm{rand}}^{\mathrm{rel}}$ is written as a sum only of volume energy changes of all inequivalent tetrahedra in a given structure. Second, the volume deformation energy for a particular tetrahedron $A_{4-n}B_n$ ($n=0,\ldots,4$) is approximated by the volume deformation energy of a crystal structure that consists exclusively of this tetrahedron type. Third, the relaxed volume of each tetrahedron type $A_{4-n}B_n$ in the random alloy at composition x is estimated from a harmonic spring model. For fcc, we have five tetrahedra corresponding to fcc (A_4), $L1_2$ (A_3B), $L1_0$ (A_2B_2), $L1_2$ (AB_3), and fcc (B_4), respectively. On the bcc lattice, there are two inequivalent forms for A_2B_2, i.e., $n=1,\ldots,6$ inequivalent tetrahedron decorations $A_{4-n}B_n$, which correspond to the six structures pure bcc (A and B), $D0_3$ (A_3B and AB_3), B2 (A_2B_2), and B32 (A_2B_2). The complete ETM expression thus resembles Eq. (13), but with the sum limited to the six specific high-symmetry configurations, and $Q_{\mathrm{rand}}(\sigma)$ replaced by the Bernoulli probability $p^{(n)}(x)$ to find a given tetrahedron decoration n at composition x

$$\delta E_{\mathrm{rand}}^{\mathrm{rel,ETM}}(x) = \sum_{n=1}^{6} p^{(n)}(x)\{E^{(n)}[V_{\mathrm{rel}}^{(n)}(x)] - E^{(n)}[V_{\mathrm{unrel}}^{(n)}(x)]\}. \quad (14)$$

Here, $V^{(n)}(x)$ denotes the volume of a tetrahedron of structure n, but equilibrated in a random alloy of volume $V_{\mathrm{rand}}(x)$. $V^{(n)}(x)$ is approximated by calculating diatomic lengths A-A, A-B, and B-B in the random medium (with bulk moduli instead of atomic force constants), and combining these to get the total volume of each tetrahedron type. $E^{(n)}[V_{\mathrm{rel}}^{(n)}(x)]$ is the value of the equation of state of structure n at the volume $V_{\mathrm{rel}}^{(n)}(x)$. $E[\boldsymbol{\sigma}_i; V_{\mathrm{unrel}}(x)]$ is the same quantity for unrelaxed random alloy. Comparing the general expression Eq. (14) to Eq. (13) of the MBCE formalism helps to reveal their important distinctions.

(a) The model of Eq. (14) includes random alloy relaxation only due to high-symmetry ordered structures bcc (A and B), $D0_3$ (A_3B and AB_3), B2 (AB), and B32 (AB), which each have an isolated, single type of local environment. In contrast, the model of Eq. (13) allows all types of ordered configurations $\boldsymbol{\sigma}$ to participate in determining relaxation energies.

(b) For ordered structures, the model of Eq. (14) does not incorporate relaxation effects that distinguish differently oriented superlattices.[20] In the ETM, this relaxation energy is zero in the long-period limit.

(c) As noted by Ruban *et al.*, the model of Eq. (14) represents the random alloy of composition x as having a *single* value of A-A relaxed interatomic distances (likewise for A-B, B-B). The general model of Eq. (13) contains contributions from a *distribution* of values for each of these bonds. This distribution can be broad.[45]

(d) The model of Eq. (14) attempts to capture all relaxation forms by volume relaxation alone, similar to the K relaxation proposed early on by Wei *et al.*[46] The general model of Eq. (13) includes all three forms of relaxation.

We may test the validity of the ETM approach by comparing with LDA: Determining relaxation energy differences for lower-symmetry structures which consist of more than one type of tetrahedron. For instance, for Mo_2Ta $C11_b$, the LDA relaxation energy $\delta E_{\mathrm{rel,LDA}}=-7.1$ meV while for $MoTa_2$ $C11_b$, $\delta E_{\mathrm{rel,LDA}}=-23.4$ meV. In the ETM, we note that the $C11_b$ unit cell consists of $2A_4+8A_3B+8A_2B_2$ tetrahedra. Using the LDA relaxed tetrahedal volumes together with LDA-derived $E(V)$ curves for A_4, A_3B, and A_2B_2 (described by the bcc, $D0_3$ and B2 structures, respectively), we arrive at $\delta E_{\mathrm{rel,ETM}}=-4.9$ meV for Mo_2Ta $C11_b$ and -5.1 meV for $MoTa_2$ $C11_b$. The obvious asymmetry in relaxation energies between Mo_2Ta and $MoTa_2$ is missed entirely by the model of Eq. (14). A failure of the ETM for relaxation energies of early transition metal impurities (specifically Nb, Mo) in Cu was already pointed out in Ref. 44, and it is possible that the failure we observed is related to those results. For the present purposes, we conclude that we require a converged expression like Eq. (13) to capture δE_{rel} correctly, rather than a limited sum based on the volume deformation of high-symmetry structures, Eq. (14).

D. Measures for the predictive power of a CE

In earlier MBCE papers,[9,10,13,16,18] problem (iv) was addressed by constructing the CE from a subset of the input LDA $\{\Delta H_f(\boldsymbol{\sigma})\}$ and using the ensuing $\{J\}$ to predict ΔH_{CE} for the remaining $\Delta H_{\mathrm{LDA}}(\boldsymbol{\sigma})$ outside the subset. The average error $\Delta H_{\mathrm{CE}} - \Delta H_{\mathrm{LDA}}$ of the predictions was then used to gauge the quality of a chosen set of interactions. In mathematical statistics, this procedure is known as "hold-out set cross-validation" (HOS-CV),[21] the hold-out set being the set of predicted LDA structures. Van de Walle and Ceder[22] have recently used "leave-one-out"(LOO) CV: Given N_σ input structures and a set of pairs and many-body interactions, N_σ successive cluster expansions are performed with only ($N_\sigma - 1$) structures in the fit, and subsequently the one left out is predicted. The LOO-CV score is the average over the prediction errors for each omitted structure. Both HOS-CV and LOO-CV have their own disadvantages. Since the configurations in the fit set are never predicted for HOS-CV, a CE selected this way will overemphasize the configurations in the prediction set at the expense of those in the input set. LOO-CV solves this problem, but on the other hand was shown by Shao[47] to favor artificially complex interaction sets.

E. Selection of input structures and interactions

Regarding point (v), the choice of pair figures is facilitated by the constrained fit Eq. (8) above. However, in earlier work[9,10,13,16,18] the choice of relevant many-body figures required tedious comparison of predicted and actual properties of an alloy to ensure that the optimum fit had been chosen. In this process, additional LDA input structures were introduced as needed, e.g., as ground-state structures of some previous prediction, but might also be excluded again if they were too high in energy and could not be fit accurately.[10]

IV. OPTIMIZED APPROACH TO THE SELECTION OF INPUT STRUCTURES AND FIGURES

A. Leave-many-out cross-validation

As mentioned above, the most promising technique to judge the predictive power of a CE from *within* a given set of input $\Delta H_{\text{LDA}}(\boldsymbol{\sigma})$ [problem (iv)] is *cross-validation*. However the two previously used approaches may either be prone to overoptimization (HOS-CV), or allow for artificial complexity of the fit (LOO-CV).[47]

To address both issues, we follow Shao's[47] suggestion and use a form of "leave-many-out" (LMO)-CV[21] to distinguish given t, λ, n_{pairs}, and the chosen $\{J_{\text{MB}}\}$. From a total N_{σ} input structures, select N_p prediction sets of N_v structures. For each set, use only the remaining $N_{\sigma} - N_v$ input structures to obtain the numerical pair and many-body interaction values which minimize s_{MBCE} of Eq. (8). Then, determine the prediction errors for the N_v validation structures from the best-fit interaction values. Here, we use $N_p \geqslant 2N_{\sigma}/N_v$ prediction sets, selected randomly with the constraint that each individual input structure appears in at least two prediction sets. Finally, the CV score is the average prediction error over the different prediction sets

$$s_{\text{cv}} = \frac{1}{bN_v} \sum_{(b \text{ sets})} \sum_{(N_v \boldsymbol{\sigma} \text{ in set})} |H_{\text{CE}}(\boldsymbol{\sigma}) - H_{\text{LDA}}(\boldsymbol{\sigma})|^2. \quad (15)$$

B. Iterative determination of input structures and figures

Our iterative algorithm to determine simultaneously both the relevant input structures and the relevant MBCE parameters $\{J\}$ is schematically outlined in Fig. 4. Given an initial LDA input set of configurations $\boldsymbol{\sigma}$, we compare s_{cv} for many different MBCE parameter sets $\{J\}$. Formally, we distinguish between different combinations of many-body terms $\{J_{\text{MB}}\}$, while $\{t, \lambda, n_{\text{pairs}}\}$ become dependent variables by minimizing s_{cv} on a three-dimensional grid. We place an additional constraint on each candidate CE: As also pointed out by van de Walle and Ceder,[22] any cross-validation score can still be subject to overoptimization by including too many free parameters for too few input structures. To address this risk, we simply limit the maximum number of many-body figures allowed in the cluster expansion. In practice, we used a maximum of five many-body figures in the final construction step of the Mo-Ta MBCE.

An important issue is the identification of those MB figures which minimize s_{cv} for a given LDA input base from the
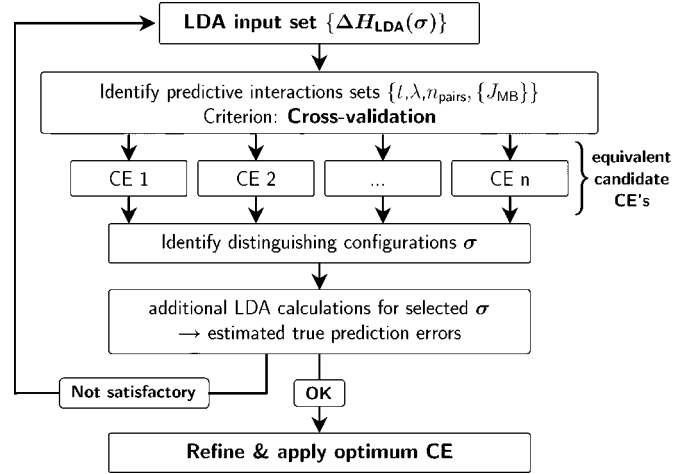

FIG. 4. Schematic flowchart of MBCE construction algorithm.

potentially infinite multitude of possible combinations. Our approach is twofold: first, we restrict the allowed many-body figures to a large but finite pool of possible candidates—in the present work, 47 MB figures (see Sec. V B). Second, we search for the optimum combination of figures for a given total number one by one, i.e., we first identify the MB figures which give best s_{cv} when fit with otherwise only pairs, J_0, and J_1 in the CE. Next, we identify a second many-body figure which gives optimum s_{cv} when included together with one of the optimum first figures, etc. This strategy has been found to work quite reliably in practice. Yet, it is not exhaustive in the sense that correlations in the search space could still be missed (e.g., the optimum set of five MB figures might not include one of the best single-MB candidates).

Normally, the result of the cross-validation analysis is not a single, "definitive" set $\{J_{\text{MB}}\}$, but rather a number of different combinations which yield similar CV scores (labeled "CE 1",..., "CE n" in Fig. 4). To further distinguish these, we investigate their *a posteriori* predictive power, by calculating additional $\Delta H_{\text{LDA}}(\boldsymbol{\sigma})$ and comparing to predicted $\Delta H_{\text{CE}}(\boldsymbol{\sigma})$. These new configurations are handpicked to best reflect the region of configuration space which we are most interested in—e.g., a number of ground-state structures predicted by the s_{cv}-equivalent CEs. If the estimated true prediction error becomes sufficiently low for the optimum CE, and the predicted ground-state line agrees with what is known from LDA within the projected error limits, we accept this combination of interaction parameters; otherwise, we add the newly calculated LDA results to the initial input set and reinitiate the construction cycle.

The resulting "optimum CE" is ready for use already at this stage. In practice, however, it is advantageous to add the newly calculated LDA results to the initial ones anyway, and refit the exact same combination of parameters for the full set of available input data, possibly using fit weights. This may further improve the CE's reproduction of particularly desirable features of configuration space.

TABLE I. Convergence of the B2 compound formation enthalpy with respect to cutoff energy E_{cut} and Monkhorst-Pack type k-space grid. The error is defined with respect to the best converged case considered, $E_{cut}=300$ eV and the $16 \times 16 \times 16$ k-space grid. Convergence is sufficient already at $E_{cut}=250$ eV and a $12 \times 12 \times 12$ grid.

E_{cut} (eV)	k mesh	ΔH_f(B2) (meV)	Error (meV)
250	$8 \times 8 \times 8$	−203.0	+1.6
250	$12 \times 12 \times 12$	−204.8	−0.2
250	$16 \times 16 \times 16$	−204.5	+0.1
300	$8 \times 8 \times 8$	−203.2	+1.4
300	$12 \times 12 \times 12$	−204.9	−0.3
300	$16 \times 16 \times 16$	−204.6	0.0

V. DETERMINISTIC CLUSTER EXPANSION OF MO-TA

A. Constructing the MBCE input: LDA calculations

To obtain the MBCE parameters defined in Eq. (3) as described in the preceding section, we require two distinct types of input from total-energy calculation: The formation enthalpies $\{\Delta H_{LDA}(\sigma)\}$ for a set of selected input configurations σ including full structural relaxation, and the corresponding constituent strain contribution $E_{ref}(\sigma)$.

Total energies E_{tot} for elemental Mo, Ta, and their compounds were obtained in the LDA to density-functional theory, using the momentum-space total-energy method[48] as implemented in the VASP program package.[49,50] Mo and Ta were represented by projector augmented wave (PAW) potentials[51,52] including $4p$ and $5p$ semicore states, respectively, together with the exchange-correlation functional of Perdew and Zunger.[53] The momentum-space basis sets (plane-wave cutoff energy E_{cut} and grid of k points) were chosen to give converged formation enthalpies of meV accuracy, as illustrated in Table I. All compound geometries were fully relaxed according to their symmetry, including both cell-external (lattice parameter and shape) and internal (atomic coordinates) degrees of freedom.

Table I gives basis set and k-point convergence tests for the simplest compound structure, B2 MoTa. These tests show $E_{cut}=250$ eV to be sufficient. Likewise, Monkhorst-Pack[54] k-point grids of $12 \times 12 \times 12$ or denser (pertaining to the cubic bcc unit cell) give sufficient accuracies wherever formation enthalpies can be calculated using equivalent k grids for elements and compounds.[55] In a few cases, the equivalent k-point method proves impractical (e.g., for 13-atom unit cells; here, k-grid convergence was achieved explicitly, using Blöchl's tetrahedron method[56] for Brillouin zone integration. The most significant approximation (except possibly LDA itself) is the use of the PAW pseudopotential approximation. For the B2 structure, the error is roughly 10 meV, or 5% with respect to all-electron LAPW calculations:[57] $\Delta H_{all\text{-}elec}=-195$ meV (LAPW) vs $\Delta H_{pseudo}=-205$ meV (PAW).

To obtain $E_{CS}(x,\hat{k})$ for the infinite superlattice limit according to Eq. (6) [and, subsequently, $E_{ref}(\sigma)$ for each configuration], we calculated the deformation energies of bcc Mo and Ta explicitly as a function of $a_{in\text{-}plane}$ and c/a, for $\hat{k}=(1,0,0)$, $(1,1,0)$, $(1,1,1)$, $(2,1,0)$, and $(3,1,1)$; for other orientations, these results were interpolated using Kubic harmonic functions.[10,16] Figure 5(a) shows the calculated constituent strain energies (infinite superlattice limit) for the five explicitly calculated orientations. For the particular case of Mo-Ta, E_{CS} is relatively small ($E_{CS} \lesssim 17$ meV) compared to typical formation enthalpies (−205 meV for B2 MoTa). It is also nearly isotropic, as reflected in the almost spherical, interpolated $E_{CS}(\hat{k})$ landscape shown in Fig. 5(b) for $x=0.5$.

B. MBCE construction for Mo-Ta

1. Cluster expansion iterations

The mixed-basis cluster expansion of Mo-Ta was created in five iterations of increasing LDA input size. The full algorithm of Sec. IV (Fig. 4) was employed from iteration 3 forward, while minor differences prevailed in iterations 1 and 2. To better illustrate the capabilities of the full strategy, we also include here MBCE's constructed for the LDA data bases of the first two iterations, obtained *a posteriori* using the exact strategy of Sec. IV. The final result (optimum CE of step 5) is independent of this history.

As described in Fig. 4, our strategy is to iteratively increase the pool of available LDA input structures. In each iteration (fixed LDA input set), several "candidate CE's" are constructed that help predict structures of interest to be calculated in LDA for the next iteration. In Appendix A, Table
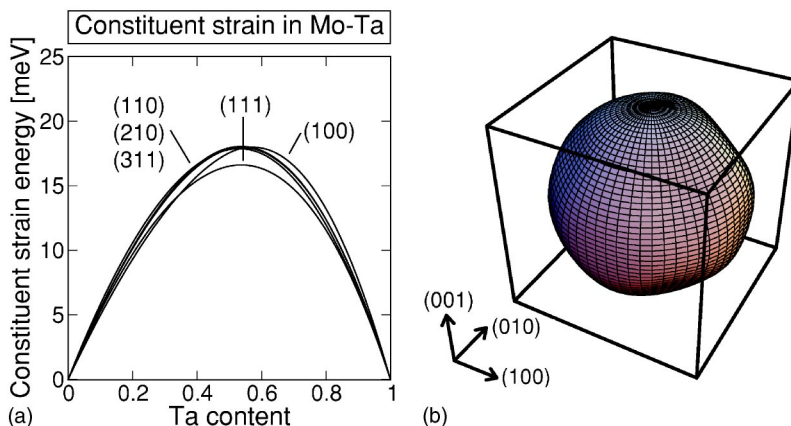

FIG. 5. (Color online) (a) Constituent strain energy $\Delta E_{CS}^{eq}(x,\hat{k})$ as a function of x for different interface orientations $\hat{k}$. (b) Polar representation of interpolated $E_{CS}^{eq}(x,\hat{k})$ as a function of $\hat{k}$ for $x=0.5$.
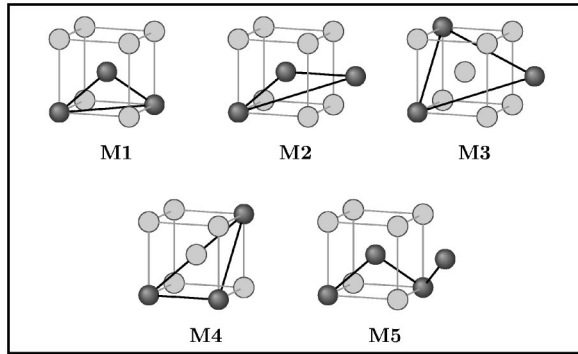
FIG. 6. Optimum many-body figures of the final MBCE iteration, extracted from a pool of 47 candidate clusters.

IV lists all LDA-calculated input structures for Mo-Ta, together with their formation enthalpies and the iteration in which they were first introduced. The input for iteration 1 consisted of a set of 24 structures, marked "1" in the last column of Table IV. In iterations 2–5, the input set was increased to 34, 43, 49, and 56 structures, respectively, with the additions in each iteration also marked in Table IV. In each iteration, the pool of many-body figures from which candidate CE's were selected comprised 47 candidate clusters: 13 inequivalent three-body terms up to fifth-nearest-neighbor maximum intersite separation, 27 inequivalent four-body figures up to fourth-nearest-neighbor maximum intersite separation, 4 inequivalent five-body figures up to third-nearest-neighbor intersite separation, and the smallest six-body figure, the octahedron (third-nearest-neighbor intersite separation). As examples, Fig. 6 shows the optimum many-body figures used for the final Mo-Ta MBCE: four three-body figures and one four-body figure, extending up to fifth-nearest-neighbor intersite separation at most. In a final step, the optimum CE of iteration 5 was refined once more using the same LDA data base, but by applying fit weights of 10 to the CE ground-state structures. This procedure improved the representation of this particularly interesting region of our without severe impact to other areas of the fit.

Figure 7 illustrates the LMO-CV score for the optimum MBCE of each iteration. LMO-CV scores for different iterations are not directly comparable numerically since the input structure set changes, and prediction sets are freshly chosen each time. Nevertheless, an interesting trend is apparent: the numerical values of s_{cv} do not fluctuate very much as the LDA structure base increases. Only the scatter of individual prediction set errors around their average is somewhat reduced.

It is interesting to compare the development of s_{cv} [Eq. (15)] to that of the least-squares fit error, s_{lsq} [Eq. (7)], tabulated in Table II for each successive iteration: s_{lsq} is always clearly smaller than s_{cv}, i.e., of little value to gauge a CE's predictive performance. To assess the latter, we can use our *a posteriori* knowledge of the complete LDA input set (Table IV in Appendix A). We may compare s_{cv} of each iteration to the averaged prediction errors for those structures not yet in the LDA data base. These values are termed s_{real} in Table II, and can be directly compared with s_{cv}. While of the same order of magnitude, s_{real} is quantitatively larger by factors
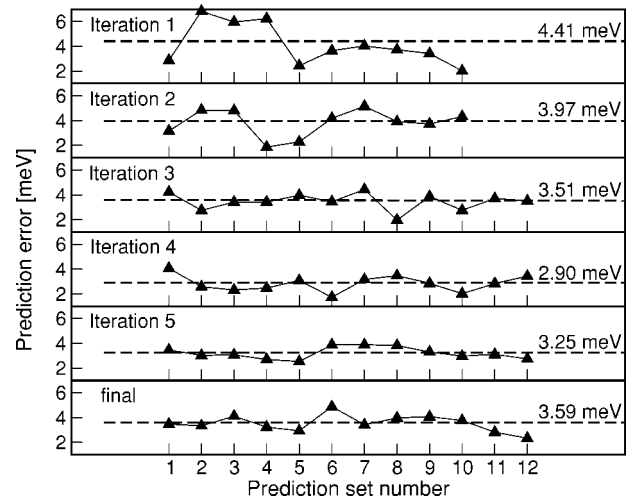

FIG. 7. Leave-many-out cross-validation for the best candidate MBCE of each iteration of the construction process. We show the prediction error for each individual set. Ten sets of five structures each (10/5) were averaged in iteration one, 10/8 in iteration 2, 12/8 in iteration 3, 12/8 in iteration 4, and 12/12 in iteration 5. Dashed lines show the average prediction error, s_{cv}, for each iteration.

1.5–2. So, s_{cv} can be used as a qualitative criterion to judge predictiveness within one iteration, but not as a quantitative one across different CE steps. For the latter purpose, knowledge of s_{real} (i.e., monitoring additional input ΔH_{LDA} after the MBCE construction in each step) is necessary.

It is apparent from Table II that s_{real} ranges up to 6 meV [i.e., 3% of the minimum $\Delta H_{LDA}(B2) = -205$ meV in the system] for the first iteration of the MBCE construction process. Hence, some average thermodynamics of Mo-Ta can be captured already with a MBCE based on the 24 initial LDA input structures. However, what is not yet captured at this stage is the alloy's ground-state line. Its development across different iterations is also summarized in Table II, for the composition range $x_{Ta} \geq 0.2$. Of the seven ground states at-

TABLE II. Performance of the cross-validation optimized CE in each iteration of the MBCE construction. s_{lsq} [Eq. (7)] is the least-squares fit error of the LDA results known in each step. s_{real} is the prediction error of all structures unknown in a particular iteration but known in the final one. Also listed is the number of ground states of the final CE which were correctly identified ("correct"), those which were not identified ("missing"), and those which were wrongly predicted ("wrong").

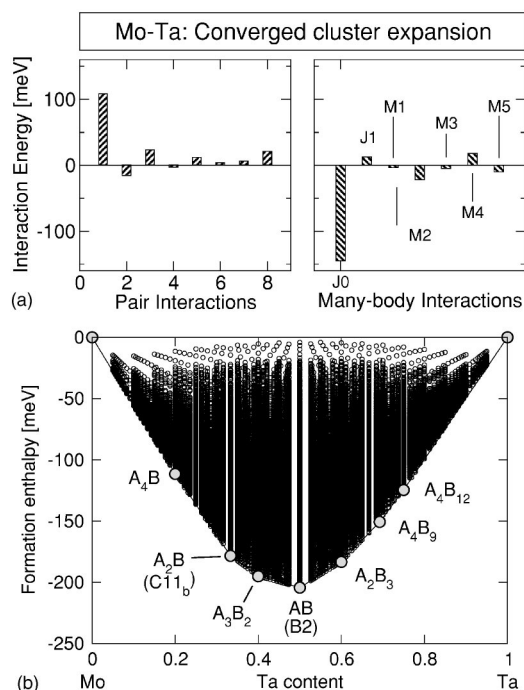| Iteration	s_{cv} (meV)	s_{lsq} (meV)	s_{real} (meV)	Ground states $\geq$20% Ta		
				Correct	Wrong	Missing
1	4.4	1.6	5.2	5	3	2
2	4.0	2.6	6.0	6	3	1
3	3.5	2.5	4.6	4	3	3
4	2.9	2.2	3.3	7	1	0
5	3.3	2.2	...	7	1	0
Final	3.6	2.5	...	7	0	0

FIG. 8. (a) Symmetry-weighted pair and many-body interactions $D_f J_f$ of the converged cluster expansion of Mo-Ta. (b) Exhaustive ground-state search (three million structures) based on the converged cluster interactions. Seven ground states are clearly identified between 20% and 80% Ta (large circles).

tested by the final CE, five are identified in the first iteration and two are missed; however, the first iteration CE predicts another three ground states which are "wrong," i.e., they are not ground states when calculated in LDA. This situation improves significantly only in iteration 4, after which one incorrect ground-state prediction remains. The latter is remedied in the final step by the application of fit weights. A sufficiently large LDA data base is necessary to capture the correct ground-state line of Mo-Ta.

2. The converged cluster expansion for Mo-Ta

The final CE for Mo-Ta employs the five MB shown in Fig. 6, and $n_{pairs}=8$ pair interactions, constrained by $t=9$ and $\lambda=4$ [Eq. (8)]. Figure 8(a) shows the symmetry-weighted interaction strengths $D_f J_f$ for the pairs and MB figures selected by the MBCE construction scheme (Sec. V B and Fig. 6). The clearly dominant interaction is an attractive nearest-neighbor term ($D_{nn} J_{nn}=108$ meV), which is more than three times stronger than any other in the system. However, the many further interactions are by no means numerically negligible. Pair interactions are of considerable magnitude up the eighth nearest neighbor ($D_{8nn} J_{8nn}=21$ meV), and at least two many-body figures (labeled M2 and M4) are of similar strength.

By all available criteria, the predictive accuracy of this CE is of the order of very few meV: The final ΔH_{CE} for all 56 input configurations compared with ΔH_{LDA} (both listed in Table IV, Appendix A) gives an average fit error $s_{lsq}=2.5$ meV and a maximum deviation of only 6.3 meV. With

$s_{cv}=3.6$ meV, its CV score (lowest panel of Fig. 7) is reassuringly small—less than 2% of ΔH_f(B2 MoTa) $=-204.8$ meV. As an additional reliability estimate, the average prediction error s_{real} between iterations 4 and 5 of the CE construction (i.e., the error of the seven LDA input structures calculated after iteration 4, when predicted by the optimum MBCE of iteration 4) amounts to 3.3 meV. The fact that s_{lsq}, s_{cv}, and s_{real} are all of the same magnitude is a good indicator for the absence of any overoptimization. The present MBCE of Mo-Ta is a reliable parametrization of the underlying LDA-PAW energetics.

The converged MBCE allows us to reexamine the short-range CE approach of Sec. II and explore the reasons for its quantitative failure. The short-range and the converged CE both identify the main qualitative feature of Mo-Ta: a strong nearest-neighbor pair interaction. However, the short-range CE neglects all other parts of the full MBCE, and its prediction errors (several tens of meV) are of the same order as the missing interactions. Beyond J_{nn}, the interactions of the short-range CE have little to do with the converged results: Its second-nearest-neighbor pair has the wrong sign, and its smallest three-body interaction is not even part of the final CE. Rather, its value is determined by the numerical necessity to compensate for the point interaction J_1. There are two obvious reasons for this wrong description of interactions. First, the number of input structures in the short-range CE is too low for the number of relevant interactions. Second, the MB interactions of the final MBCE would be impossible to guess from intuition alone. Overcoming both obstacles necessitates a systematic construction algorithm, such as described above.

VI. RESULTS: GROUND STATES AND ALLOY THERMODYNAMICS

A. Ground-state structures

Figure 8(b) shows the $\Delta H_{CE}(\sigma)$ versus the concentration map of all three million structures with bcc-based supercells up to 20 atoms. As in Sec. II, ground states can be read from this plot as the breaking points of the convex hull about all structures. There are seven distinct deep breaking points in Fig. 8(b). Full atomic coordinate sets as computed by VASP can be found in Appendix C. The five distinct small-cell ground states between 20% and 60% Ta are all superlattice sequences of (100) atomic planes: A_4B, A_2B (C11$_b$), A_3B_2, AB (B2), and A_2B_3. They are contrasted by two much more complex Ta-rich nonsuperlattice structures, A_4B_9 and A_4B_{12}. An in-depth discussion of these structures and their intermediate regions is given in Ref. 23. The unexpectedly feature-rich ground-state line of Mo-Ta emphasizes the power of a systematically constructed MBCE. Five of these structures are true *predictions* of the MBCE construction process, and only subsequently confirmed by direct LDA calculations. Simply guessing this variety of atomic arrangements from an intuition-based, short-range CE approach (Sec. II) is practically impossible.

B. Order-disorder transitions of Mo-Ta

In the approximation of nearest-neighbor interactions only, the transition between the ordered B2 and disordered
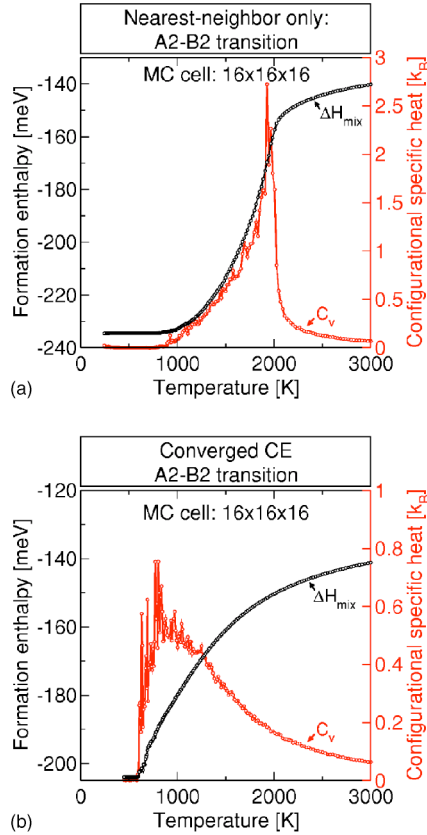
TABLE III. Critical temperatures of ordered ground states from
Monte Carlo simulations (cell sizes $20 \times 20 \times 20$ and above).

Ground state	Transition to	T_c (K)	Transition to	T_c (K)
A_4B	A2	195		
A_2B	B2	400	A2	560
A_3B_2	B2	275	A2	550
AB	A2	$600-1000$[a]		
A_2B_3	A2	610		
A_4B_9	A2	490		
A_4B_{12}	A2	385		

[a]Second-order transition.

FIG. 9. (Color online) (a) Monte Carlo simulation of the classic
A2-B2 transition in the nearest-neighbor-only approximation, using
J_{nn} of the full Mo-Ta MBCE. (b) Same, but using all interactions of
the full MBCE for Mo-Ta.

A2 states is theoretically well understood as a model second-order transition. For this case, both the analytic (series-expansion) limit[58] and early Monte Carlo simulations[59] agree on a transition temperature $k_BT_c = 6.35J_{nn}$. Since the nearest neighbor interaction J_{nn} is the clearly dominant term of our Mo-Ta MBCE [Fig. 8(a)], it would seem natural that a simple nearest-neighbor-only formula should give a good idea of the true A2-B2 T_c. In this approximation, $D_{nn}J_{nn} = 108$ meV of Mo-Ta corresponds to a T_c of almost 2000 K. This conflicts with experiment, since the published phase diagram reports only a continuous A2 solid solution, and early x-ray diffraction measurements[60] revealed no super-structure for samples sintered either at 1773 K (5 h) or 673 K (100 h). Ordering might have been inhibited at 673 K since diffusion in Mo-Ta is slow,[61] but should have been sufficiently fast at 1773 K.

This failure can be related to the neglected high-order pair and many-body interactions of real Mo-Ta. To verify this, we performed canonical Monte Carlo simulations using our converged MBCE Hamiltonian. We used $Mo_{0.5}Ta_{0.5}$ supercells sized up to $32 \times 32 \times 32$ unit cells, cooling down stepwise from the high-T solid solution into the B2-ordered regime, with 2000 or 4000 spin flips per site and step for proper equilibration. Figure 9 displays the resulting mixing enthalpy ΔH_{CE} and the configurational heat capacity C_v for $16 \times 16 \times 16$ supercells. The Monte Carlo simulation agrees with

Ref. 59 when restricted to the nearest-neighbor-only approximation [Fig. 9(a)]: As expected for a second-order transition, $\Delta H_{nn\text{-}only}$ varies smoothly with T, and a clear peak in the specific heat indicates $T_c = 1980 \pm 50$ K. In striking contrast, the maximum of C_v is located around 800 K for the *full* Mo-Ta CE [Fig. 9(b)], more than a factor of 2 below the short-range approximation. The transition is still of second order, but the presence of additional high-order pair and MB figures leads to a dramatic slowdown. Once more, the use of a short-range approximation proves severely dangerous, and underlines the need for a full MBCE even for qualitative purposes.

Table III lists critical temperatures, i.e., the upper limits of thermodynamic stability, also for the remaining ground states of Mo-Ta. In each case, supercell sizes above $20 \times 20 \times 20$ were found sufficiently accurate, and clearly pinpointed first-order transitions occur everywhere but for B2. Reassuringly, all ordered ground states are thermodynamically stable only well below 1000 K. Additionally, the canonical MC simulations suggest an extension of B2 long-range order to the Mo-rich side at finite T. Both the $C11_b$ and A_3B_2 ground states transition into a B2 arrangement with one disordered Ta-rich sublattice rather than directly into A2. For fixed concentration and accessible cell sizes, possible interfacial effects preclude a definitive conclusion on whether the disordered B2 area prevails also in the thermodynamic limit, or whether a phase-separated A2-B2 regime could provide an even lower free energy on a very large scale. In any case, the full MBCE predicts all transitions well below the temperature range assessed in earlier experiments, and thus yields a consistent picture of Mo-Ta.

C. Mixing enthalpies

The MBCE also allows us to investigate finite-T energetics of the A2 solid solution. In the fully random limit ($T \to \infty$), the mixing enthalpy $\Delta H_{mix}(x, T)$ is given analytically by inserting correlation function averages over all configurations $\boldsymbol{\sigma}$ at fixed composition x into the MBCE Hamiltonian Eq. (3). Since $\langle \bar{\Pi}_f \rangle_{\sigma}|_x = (2x-1)^l$ for figures f with l vertices, we obtain[20]
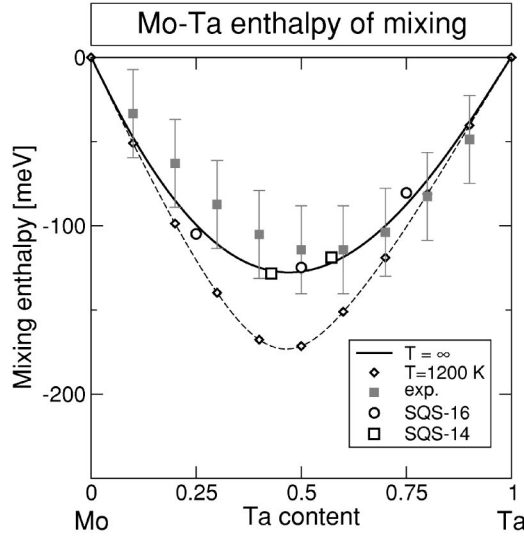
FIG. 10. Enthalpy of mixing of the random alloy ("$T=\infty$") and at 1200 K, predicted from the converged MBCE and compared to experimental data points (Ref. 25). For comparison, direct LDA calculations for special quasirandom structures are also shown.

$$\Delta H_{\mathrm{mix}}(x,\infty) = J_0 + (2x-1)J_1 + \sum_{\mathrm{pairs}} (2x-1)^2 D_{\mathrm{pair}} J_{\mathrm{pair}}$$

$$+ \sum_{\mathrm{MBs}} (2x-1)^l D_{\mathrm{MB}} J_{\mathrm{MB}} + \int_\Omega \Delta E_{\mathrm{CS}}^{\mathrm{eq}}(\hat{k},x) d^2\hat{k}. \quad (16)$$

This predicted functional dependence of $\Delta H_{\mathrm{mix}}(\infty)$ on x is shown in Fig. 10. It is almost symmetric, with minimum $\Delta H_{\mathrm{mix}} = -127$ meV at $x=0.47$.

To verify the magnitude and slight degree of asymmetry of ΔH_{mix} we performed additional *direct* LDA calculations, modeling the random alloy limit by quasirandom structures, which mimic $\bar{\Pi}_f = (2x-1)^l$ for short-ranged figures as closely as possible. Figure 10 includes results for special quasirandom structures[62] $\mathrm{Mo}_{1-x}\mathrm{Ta}_x$ with 16 atoms per unit cell (SQS-16) and $x=0.25$, 0.5, and 0.75, which fullfill $\bar{\Pi}_p = (2x-1)^2$ *exactly* for at least the first four pairs. For other concentrations, meeting even only $\bar{\Pi}_{\mathrm{nn}} = (2x-1)^2$ exactly is not always possible, i.e., *strict* SQS cannot be constructed. To capture the range closer to $x=50\%$ in direct LDA calculations anyway, we define 14-atom structures $\mathrm{Mo}_8\mathrm{Ta}_6$ and $\mathrm{Mo}_6\mathrm{Ta}_8$ (dubbed "SQS-14") which minimize $\sum_f |\bar{\Pi}_f(\boldsymbol{\sigma}) - (2x-1)^l|^2$ for a certain number of local figures (here, the first ten pairs, and three- and four-body figures up to a maximum vertex distance of third-nearest pairs). Appendix D gives the structure of SQS-16 and SQS-14. As can be seen in Fig. 10, their directly calculated formation enthalpies coincide quantitatively with both the magnitude and tentative asymmetry of the MBCE-predicted $\Delta H_{\mathrm{mix}}(x,\infty)$—the converged MBCE provides a reliable mapping of LDA. The general magnitude of $\Delta H_{\mathrm{mix}}(x,\infty)$ is also in line with the only available experiment,[25] as well as earlier semiempirical calculations.[28–30,63,64] The experimental data is plotted to-

gether with our data in Fig. 10; at face value, the experimental error limits cover our prediction well.

To quantify the impact of short-range order in the solid solution at finite T, we performed another set of canonical Monte Carlo simulations at fixed $T=1200$ K, and across the entire concentration range in steps of 10%. The resulting $\Delta H_{\mathrm{mix}}(x,1200\ \mathrm{K})$, also shown in Fig. 10, lies below the random limit by up to 50 meV. Short-range order is a strong effect in Mo-Ta, even clearly above the T range of long-range order formation. However, $T=1200$ K is also the very temperature to which the above-cited experimental data correspond. If so, our $T=1200$ K prediction underestimates the truth substantially. In principle, this could be a systematic error of LDA; however, a quick test for the B2 structure shows that $\Delta H(\mathrm{B2}) = -199$ meV in the Perdew-Wang generalized-gradient approximation,[65] only 6 meV away from the LDA result (Table I). On the other hand, it is unclear how the sample was equilibrated in Ref. 25 and whether true *configurational* equilibrium (which requires long diffusion times) was ever attained. In any event, the MBCE Hamiltonian achieves our stated goal of representing the energetics of full-scale LDA calculations with reassuring accuracy.

D. Short-range order

Monte Carlo simulations also provide the actual atomic distribution of the Mo-Ta solid solution at 1200 K. By convention, short-range order is visualized through pair correlations in reciprocal space, since these determine the chemical contribution to experimental diffuse diffraction intensities

$$\alpha_{\mathrm{SRO}}(x,\boldsymbol{k}) = \sum_{n=1}^{n_R} \alpha_{\mathrm{SRO}}(x,n) e^{i\boldsymbol{k}\boldsymbol{R}_n}, \quad (17)$$

where $\boldsymbol{R}_n$ is the real-space vector of pair n, $n_{\boldsymbol{R}}$ is a sufficiently high real-space cutoff, and

$$\alpha(x,n) = \frac{\bar{\Pi}_{\mathrm{pair}\ n} - (2x-1)^2}{1 - (2x-1)^2}. \quad (18)$$

For $x=0.2$, 0.4, and 0.9, Fig. 11 plots the predicted $\alpha_{\mathrm{SRO}}(x,\boldsymbol{k})$ at $T=1200$ K in a (100) section through reciprocal space. As anticipated from ΔH_{mix}, short-range order is a strong effect in the Mo-Ta solid solution. At $x=0.2$, the main feature is a single peak centered about (100), consistent with the (100) superlattice structural motif. This structure is dominant also at $x=0.4$, but it is now topped by a very narrow, ringlike structure around the (100) point itself—possibly indicative of a tendency for antiphase domains of local order. In sharp contrast, $\alpha_{\mathrm{SRO}}(x,\boldsymbol{k})$ ($x=0.9$) is much weaker in the Ta-rich limit. The intensity at (100) itself is zero, and replaced by a low, extended ring in the plane of interest. It is interesting to compare this to the prediction of the short-ranged real-space CE in Sec. II. At $x=0.2$ and 0.9, this would yield a simple sharp peak around (100). At $x=0.4$ and $T=1200$ K, our calculations show that the material would already exhibit B2-like long-range order, since T_c for the short-ranged real-space CE is close to that obtained for stoichio-
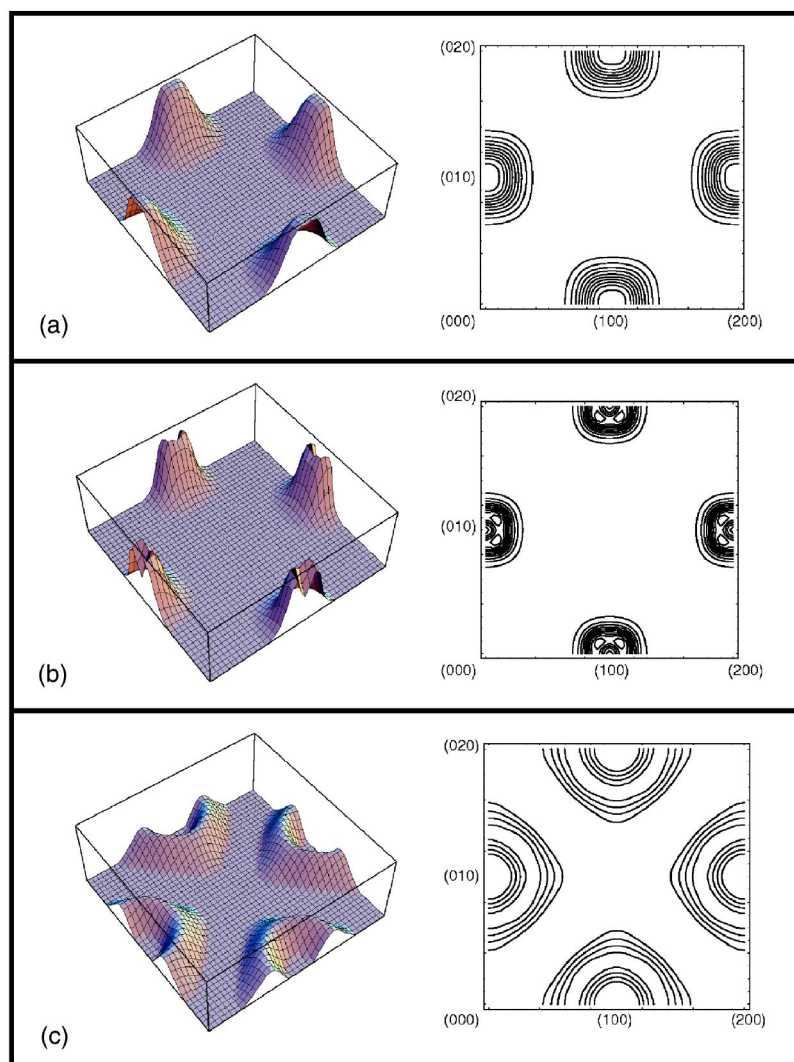
FIG. 11. (Color online) Predicted short-range order of Mo-Ta alloys at $T=1200$ K for (a) $x=0.2$, (b) $x=0.4$, (c) $x=0.9$ in the (001) plane of reciprocal space. Monte Carlo cell size: $20\times20\times20$, equilibration: 8000 flips/site total.

metric B2 MoTa and a nearest-neighbor-only model in Fig. 9(a).

Experimentally, diffuse intensity measurements along the (000)-(400) line on Mo-Ta for $x=21\%$, 37%, and 91% have been reported by Predmore and Arsenault.[24] These authors presented uncorrected diffraction data (i.e., α_{SRO} is overlaid by fundamental Bragg peaks, thermal scattering, lattice distortion, etc.), and did not specify a temperature of equilibration, so that we may only attempt a qualitative comparison with our predictions. Still, this comparison is quite favorable: At $x=21\%$ and 37%, clear peaks at roughly (100) positions in reciprocal space are found by Predmore and Arsenault, very similar to those predicted by us at $x=0.2$ and 0.4. In contrast, no strong (100)-centered peak is apparent for the 91% sample. Instead, there is a low, bulgelike structure somewhat off the (100) position—again, very consistent with our findings at $x=0.9$. The finite-T behavior of Mo-Ta is convincingly represented by our MBCE Hamiltonian.

VII. CONCLUSIONS

We have presented a consistent, deterministic approach to map a first-principles configurational Hamiltonian onto an Ising-like model Hamiltonian in the framework of the MBCE method. For the example of Mo-Ta, we show that a short-range, "intuition-based" cluster expansion approach is quantitatively insufficient—it misses essential features, both with respect to ground states and finite-T thermodynamics (transition temperatures). In contrast, our converged MBCE Hamiltonian identifies ground states of a complexity not anticipated in body-centered cubic alloys, finds low transition temperatures that are compatible with the experimental absence of long-range ordered phases, describes short-range order in the solid solution consistent with earlier experiments, and finally allows to extract finite-T energetics up to the fully random alloy limit with LDA quality.

APPENDIX A: LISTING OF LDA INPUT DATA USED IN THE MO-TA MBCE

Table IV lists formation enthalpies for the 56 fully relaxed input structures which were used as a basis for the

TABLE IV. Formation enthalpies of the 56 LDA input structures used for Mo-Ta, and best-fit ΔH_{CE} of the converged CE.

Composition	Structure	ΔH_{LDA} (meV)	ΔH_{CE} (meV)	First present (iter.)
Mo	A2	0.0	0.9	1
Mo_8Ta	"A_8B" (App. B)	−66.3	−60.9	2
Mo_7Ta	(210) A_7B SL	−63.3	−65.7	2
	"A_7B" (App. B)	−65.4	−64.3	5
Mo_6Ta	(100) A_6B SL	−78.0	−79.1	3
	(111) A_6B SL	−74.3	−74.6	5
Mo_5Ta	(433) A_8BA_2B SL	−86.6	−88.7	3
Mo_4Ta	(111) A_4B SL	−103.1	−101.3	3
	(100) A_4B SL	−111.1	−111.5	5
	(310) A_4B SL	−107.0	−103.1	5
Mo_3Ta	$D0_3$	−128.9	−128.5	1
	$L6_0$	−128.7	−124.7	1
	(100) A_3B SL	−134.6	−131.8	1
	(110) A_3B SL	−77.5	−79.7	1
	(310) A_3B SL	−132.0	−129.3	1
	"$A_{12}B_4$-I" (App. B)	−125.9	−129.2	2
	"A_4B_{12}" (App. C)	−130.9	−134.5	4
	"$A_{12}B_4$-II" (App. B)	−128.4	−130.9	4
Mo_5Ta_2	(100) A_3BA_2B SL	−150.8	−151.7	3
	(111) A_4BAB SL	−148.8	−146.9	3
Mo_2Ta	$C11_b$	−179.1	−178.4	1
	(110) A_2B SL	−101.0	−101.9	1
	(111) A_2B SL	−119.4	−119.2	1
Mo_9Ta_5	(710) $A_4B_3A_4BAB$ SL	−175.6	−180.5	2
Mo_5Ta_3	(210) $A_3B(AB)_2$ SL	−180.5	−180.3	2
Mo_3Ta_2	(210) $A_3B(AB)_3$ SL	−181.8	−186.8	2
	(111) A_2BAB SL	−177.4	−179.5	3
	(100) A_2BAB SL	−195.6	−195.1	4
Mo_4Ta_3	(100) $A_2B(AB)_2$ SL	−196.0	−197.6	3
	(111) $A_2B(AB)_2$ SL	−193.8	−195.2	3
MoTa	A_1	−117.6	−117.4	1
	B2	−204.8	−204.4	1
	B11	−147.5	−144.5	1
	B32	−110.8	−109.1	1
	(110) A_2B_2 SL	−86.0	−86.9	1
	(310) A_2B_2 SL	−191.9	−193.8	1
	"A_8B_8" (App. B)	−135.3	−135.7	4
Mo_3Ta_4	(100) $A_2B(AB)_2$ SL	−183.6	−189.2	3
	(111) $A_2B(AB)_2$ SL	−186.0	−185.6	4
Mo_2Ta_3	(100) A_2BAB SL	−180.1	−183.4	2
$MoTa_2$	$C11_b$	−157.6	−159.2	1
	(110) AB_2 SL	−86.6	−84.1	1
	(111) AB_2 SL	−105.6	−108.2	1
Mo_4Ta_9	"A_4B_9" (App. C)	−153.5	−150.7	5
$MoTa_3$	$D0_3$	−79.4	−82.2	1
	$L6_0$	−80.5	−81.4	1
	(100) AB_3 SL	−105.6	−101.3	1

TABLE IV. (*Continued.*)

Composition	Structure	ΔH_{LDA} (meV)	ΔH_{CE} (meV)	First present (iter.)
	(110) AB_3 SL	−63.9	−65.7	1
	(310) AB_3 SL	−113.3	−116.4	1
	"A_4B_{12}" (App. C)	−125.7	−124.6	2
	"$A_{12}B_4$-II" (App. B)	−97.8	−96.5	4
$MoTa_4$	(100) A_4B SL	−84.6	−86.4	5
	(310) A_4B SL	−92.8	−99.1	5
$MoTa_7$	(210) A_7B SL	−51.3	−51.8	2
$MoTa_8$	"A_8B" (App. B)	−44.0	−48.6	2
Ta	A2	0.0	1.1	1

cluster expansion of Mo-Ta. Both direct LDA calculations and the fitted cluster expansion formation enthalpies are listed. Structures are defined either by a common name, or in a superlattice notation. For the cases where neither nomenclature exists, the actual lattice occupation is described in Appendix B.

APPENDIX B: DEFINITION OF NONSUPERLATTICE LDA INPUT STRUCTURES IN TABLE IV

The present section defines those LDA input structures (Table IV) which have no common name, and cannot be described by a superlattice notation. To emphasize the connection between superstructure and underlying bcc lattice, atomic coordinates are given in Cartesian coordinates, in units of the (cubic) bcc lattice parameter, and without relaxation.

1. A_8B

Description: This structure is a body-centered tetragonal "$3 \times 3 \times 1$" defect cell of minority atoms embedded in the majority matrix.

Space group: $I4/mmm$ (No. 139 in the International Tables for Crystallography[66]).

Primitive cell (Cartesian coordinates):
$a_1=(1.0,0.0,0.0)$, $a_2=(0.5,1.5,1.5)$, $a_3=(0.5,-1.5,1.5)$
Atomic coordinates (Cartesian coordinates):
A_1:(1.0,−1.0,1.0), A_2:(0.5,−0.5,0.5), A_3:(0.5,0.5,0.5), A_4:(0.5,−0.5,1.5), A_5:(1.0,0.0,1.0), A_6:(1.0,1.0,1.0), A_7:(1.0,0.0,2.0), A_8:(0.5,0.5,1.5), B_1:(0.0,0.0,0.0).

2. A_7B

Description: This structure is a primitive tetragonal defect cell of minority atoms embedded in the majority matrix, in a sequence of one $c(2\times2)$ (100) AB plane followed by three pure A planes.

Space group: $P4/mmm$ (No. 123 in the International Tables for Crystallography[66]).

Primitive cell (Cartesian coordinates):
$a_1=(1.0,-1.0,1.0)$, $a_2=(1.0,1.0,0.0)$, $a_3=(0.0,0.0,2.0)$
Atomic coordinates (Cartesian coordinates):

A_1:(1.0,0.0,0.0), A_2:(0.5,−0.5,0.5), A_3:(0.5,0.5,0.5), A_4:(0.0,0.0,1.0), A_5:(1.0,0.0,1.0), A_6:(0.5,−0.5,1.5), A_7:(0.5,0.5,1.5), B_1:(0.0,0.0,0.0).

3. $A_{12}B_4$-I

Description: This is a body-centered tetragonal structure of (100)-oriented, pure B, and alternating AB columns embedded into an A matrix.

Space group: $I4_1/amd$ (No. 141 in the International Tables for Crystallography[66]).

Primitive cell (Cartesian coordinates):
$a_1=(2.0,0.0,0.0)$, $a_2=(0.0,2.0,0.0)$, $a_3=(1.0,1.0,2.0)$
Atomic coordinates (Cartesian coordinates):
A_1:(0.0,1.0,0.0), A_2:(1.0,1.0,0.0), A_3:(0.5,0.5,0.5), A_4:(0.5,1.5,0.5), A_5:(1.5,0.5,0.5), A_6:(1.5,1.5,0.5), A_7:(2.0,1.0,1.0), A_8:(2.0,2.0,1.0), A_9:(1.5,1.5,1.5), A_{10}:(2.5,2.5,1.5), A_{11}:(2.5,1.5,1.5), A_{12}:(1.5,2.5,1.5), B_1:(0.0,0.0,0.0), B_2:(1.0,0.0,0.0), B_3:(1.0,1.0,1.0), B_4:(1.0,2.0,1.0).

4. $A_{12}B_4$-II

Description: This is a cubic structure with $(2\times2\times2)$ unit cell.

Space group: $Pm\bar{3}m$ (No. 221 in the International Tables for Crystallography[66]).

Primitive cell (Cartesian coordinates):
$a_1=(2.0,0.0,0.0)$, $a_2=(0.0,2.0,0.0)$, $a_3=(0.0,0.0,2.0)$
Atomic coordinates (Cartesian coordinates):
A_1:(1.0,1.0,0.0), A_2:(0.5,0.5,0.5), A_3:(1.5,0.5,0.5), A_4:(0.5,1.5,0.5), A_5:(1.5,1.5,0.5), A_6:(1.0,0.0,1.0), A_7:(0.0,1.0,1.0), A_8:(1.0,1.0,1.0), A_9:(0.5,0.5,1.5), A_{10}:(1.5,0.5,1.5), A_{11}:(0.5,1.5,1.5), A_{12}:(1.5,1.5,1.5), B_1:(0.0,0.0,0.0), B_2:(1.0,0.0,0.0), B_3:(0.0,1.0,0.0), B_4:(0.0,0.0,1.0).

5. A_8B_8

Description: This structure has a $(2\times2\times2)$ primitive cubic unit cell, but is of trigonal symmetry due to the unit cell's atomic content.

Space group: $R\bar{3}m$ (No. 166 in the International Tables for Crystallography[66]).

Primitive cell (Cartesian coordinates):
$a_1 = (2.0, 0.0, 0.0)$, $a_2 = (0.0, 2.0, 0.0)$, $a_3 = (0.0, 0.0, 2.0)$

Atomic coordinates (Cartesian coordinates):
A_1: (1.0, 1.0, 1.0), A_2: (1.5, 1.5, 0.5), A_3: (1.5, 0.5, 1.5),
A_4: (0.0, 1.0, 0.0), A_5: (0.5, 1.5, 1.5), A_6: (1.0, 0.0, 1.0),
A_7: (1.0, 1.0, 0.0), A_8: (1.5, 1.5, 1.5), B_1: (0.0, 0.0, 0.0),
B_2: (0.5, 0.5, 1.5), B_3: (0.5, 1.5, 0.5), B_4: (1.0, 0.0, 0.0),
B_5: (1.5, 0.5, 0.5), B_6: (0.0, 1.0, 0.0), B_7: (0.0, 0.0, 1.0),
B_8: (0.5, 0.5, 0.5).

APPENDIX C: ATOMIC COORDINATES OF THE PREDICTED MO-TA GROUND-STATE STRUCTURES

The present section lists fully relaxed atomic coordinates for each ground-state structure identified in Mo-Ta as calculated by VASP.[49,50] Since these are actual structures that could be found in experiment, the full crystallographic notation is used rather than the notation in Cartesian coordinates. In addition, Pearson symbols[67] are listed for each structure.

1. Mo$_4$Ta

Description: This structure is best visualized as an A_4B sequence (superlattice) of (100) atomic planes. It has a body-centered tetragonal cell.

Space group: $I4/mmm$ (No. 139 in the International Tables for Crystallography[66]).

Pearson symbol: $tI10$

Unit-cell parameters (primitive cell):
$a = 3.140$ Å, $b = 3.140$ Å, $c = 8.190$ Å
$\alpha = 78.95°$, $\beta = 78.95°$, $\gamma = 90.00°$

Fractional atomic coordinates:
Mo$_1$: (0.397, 0.397, 0.206),   Mo$_2$: (0.800, 0.800, 0.399),
Mo$_3$: (0.200, 0.200, 0.601),   Mo$_4$: (0.603, 0.603, 0.794),
Ta$_1$: (0.000, 0.000, 0.000).

2. Mo$_2$Ta

Description: This is the C11$_b$ structure, best visualized as an A_2B sequence (superlattice) of (100) atomic planes. It has a body-centered tetragonal cell.

Space group: $I4/mmm$ (No. 139 in the International Tables for Crystallography[66]).

Pearson symbol: $tI6$

Unit cell parameters (primitive cell):
$a = 3.152$ Å, $b = 3.152$ Å, $c = 5.250$ Å
$\alpha = 72.53°$, $\beta = 72.53°$, $\gamma = 90.00°$

Fractional atomic coordinates:
Mo$_1$: (0.330, 0.330, 0.339),   Mo$_2$: (0.670, 0.670, 0.661),
Ta$_1$: (0.000, 0.000, 0.000).

3. Mo$_3$Ta$_2$

Description: This structure is best visualized as an A_2BAB sequence (superlattice) of (100) atomic planes. It has a body-centered tetragonal cell.

Space group: $I4/mmm$ (No. 139 in the International Tables for Crystallography[66]).

Pearson symbol: $tI10$
Unit-cell parameters (primitive cell):
$a = 3.161$ Å, $b = 3.161$ Å, $c = 8.1246$ Å
$\alpha = 78.95°$, $\beta = 78.95°$, $\gamma = 78.95°$
Fractional atomic coordinates:
Mo$_1$: (0.000, 0.000, 0.000),   Mo$_2$: (0.797, 0.797, 0.406),
Mo$_3$: (0.203, 0.203, 0.594),   Ta$_1$: (0.401, 0.401, 0.199),
Ta$_2$: (0.599, 0.599, 0.801).

4. MoTa

Description: This is the B2 structure, the AB sequence (superlattice) of (100) atomic planes. It has a cubic cell.

Space group: $Pm\bar{3}m$ (No. 221 in the International Tables for Crystallography[66]).

Pearson symbol: $cP2$

Unit-cell parameters (primitive cell):
$a = 3.177$ Å, $b = 3.177$ Å, $c = 3.177$ Å
$\alpha = 90.00°$, $\beta = 90.00°$, $\gamma = 90.00°$

Fractional atomic coordinates:
Mo$_1$: (0.000, 0.000, 0.000), Ta$_1$: (0.500, 0.500, 0.500).

5. Mo$_2$Ta$_3$

Description: This structure is best visualized as an A_2BAB sequence (superlattice) of (100) atomic planes. It has a body-centered tetragonal cell.

Space group: $I4/mmm$ (No. 139 in the International Tables for Crystallography[66]).

Pearson symbol: $tI10$

Unit-cell parameters (primitive cell):
$a = 3.161$ Å, $b = 3.161$ Å, $c = 8.1246$ Å
$\alpha = 78.95°$, $\beta = 78.95°$, $\gamma = 90.00°$

Fractional atomic coordinates:
Mo$_1$: (0.000, 0.000, 0.000),   Mo$_2$: (0.797, 0.797, 0.406),
Mo$_3$: (0.203, 0.203, 0.594),   Ta$_1$: (0.401, 0.401, 0.199),
Ta$_2$: (0.599, 0.599, 0.801).

6. Mo$_4$Ta$_9$

Description: This structure can be described as an $A_6B_2A_3B_2$ sequence (superlattice) of (510) atomic planes. It has a body-centered tetragonal cell. The unit cell is that of Ga$_4$Sm$_9$, but the occupation of sites is different.

Space group: $I4/m$ (No. 87 in the International Tables for Crystallography[66]).

Pearson symbol: $tI26$

Unit-cell parameters (primitive cell):
$a = 8.345$ Å, $b = 8.345$ Å, $c = 3.194$ Å
$\alpha = 78.97°$, $\beta = 78.97°$, $\gamma = 87.90°$

Fractional atomic coordinates:
Mo$_1$: (0.780, 0.157, 0.531),   Mo$_2$: (0.856, 0.772, 0.686),
Mo$_3$: (0.394, 0.082, 0.762),   Mo$_4$: (0.470, 0.696, 0.917),
Ta$_1$: (0.000, 0.000, 0.000),   Ta$_2$: (0.551, 0.302, 0.073),
Ta$_3$: (0.077, 0.622, 0.150),   Ta$_4$: (0.625, 0.927, 0.224),
Ta$_5$: (0.173, 0.231, 0.298),   Ta$_6$: (0.698, 0.551, 0.375),
Ta$_7$: (0.249, 0.854, 0.449),   Ta$_8$: (0.320, 0.475, 0.602),
Ta$_9$: (0.929, 0.379, 0.846).

7. Mo_4Ta_{12}

Description: This structure can not be described by a superlattice notation. It has a simple tetragonal cell.

Space group: $P4_2/mnm$ (No. 136 in the International Tables for Crystallography[66]).

Pearson symbol: $tP24$

Unit-cell parameters (primitive cell):

$a=3.178$ Å, $b=9.152$ Å, $c=9.152$ Å

$\alpha=90.00°$, $\beta=90.00°$, $\gamma=90.00°$

Fractional atomic coordinates:

Mo_1: (0.000,0.001,0.001), Mo_2: (0.000,0.749,0.749), Mo_3: (0.500,0.249,0.501), Mo_4: (0.500,0.501,0.249), Ta_1: (0.000,0.008,0.497), Ta_2: (0.000,0.253,0.742), Ta_3: (0.000,0.255,0.255), Ta_4: (0.000,0.495,0.495), Ta_5: (0.000,0.497,0.008), Ta_6: (0.000,0.742,0.253), Ta_7: (0.500,0.242,0.997), Ta_8: (0.500,0.508,0.753), Ta_9: (0.500,0.753,0.508), Ta_{10}: (0.500,0.755,0.995), Ta_{11}: (0.500,0.995,0.755), Ta_{12}: (0.500,0.997,0.242).

APPENDIX D: DEFINITION OF BCC SPECIAL QUASIRANDOM STRUCTURES

The present section defines the body-centered cubic (special) quasirandom structures used to verify the MBCE-predicted random alloy enthalpy of mixing in Sec. VI C (Fig. 10). To emphasize the connection between superstructure and underlying bcc lattice, atomic coordinates are given in Cartesian coordinates, in units of the (cubic) bcc lattice parameter, and without relaxation.

1. SQS-16 $A_{0.75}B_{0.25}$

Description: This is the only bcc-based structure with 16 atoms per unit cell and $x=25$ which satisfies $\Pi_p(\boldsymbol{\sigma})=0.25$ for the first four pair correlation functions. It has a base-centered monoclinic unit cell.

Space group: Cm (No. 8 in the International Tables for Crystallography[66]).

Primitive cell (Cartesian coordinates):

$a_1=(2.1,-2.0,0.0)$, $a_2=(1.0,1.0,0.0)$, $a_3=(1.0,0.0,2.0)$

Atomic coordinates (Cartesian coordinates):

A_1: (1.0,0.0,0.0), A_2: (1.0,−1.0,0.0), A_3: (2.0, −1.0,0.0), A_4: (2.5,−1.5,0.5), A_5: (2.5,−0.5,0.5), A_6: (2.0,−1.0,1.0), A_7: (2.0,0.0,1.0), A_8: (3.0,−1.0,1.0), A_9: (1.5,−0.5,1.5), A_{10}: (1.5,0.5,1.5), A_{11}: (2.5, −1.5,1.5), A_{12}: (2.5,−0.5,1.5), B_1: (0.0,0.0,0.0), B_2: (1.5,−0.5,0.5), B_3: (1.5,0.5,0.5), B_4: (1.0,0.0,1.0).

2. SQS-16 $A_{0.50}B_{0.50}$

Description: There are no structures with less than 16 atoms per unit cell and $x=0.5$ which satisfy $\Pi_p(\boldsymbol{\sigma})=0.0$ for the first five pair correlation functions, but twelve different 16-atom structures satisfy this criterion. The SQS selected here is subject to the additional criterion that the least-squares sum over some of the remaining, nonzero short-range correlation functions (first ten pair shells, and three- and four-body figures up to third-nearest-neighbor maximum vertex distance) is minimal. It is a triclinic structure.

Space group: $P1$ (No. 1 in the International Tables for Crystallography[66]).

Primitive cell (Cartesian coordinates):

$a_1=(1.5,0.5,0.5)$, $a_2=(1.0,-1.0,-1.0)$, $a_3=(0.5,1.5, -2.5)$

Atomic coordinates (Cartesian coordinates):

A_1: (0.5,0.5,−0.5), A_2: (1.0,1.0,−1.0), A_3: (1.5,0.5, −1.5), A_4: (1.5,0.5,−1.5), A_5: (1.5,0.0,−1.0), A_6: (1.0,0.0,−2.0), A_7: (1.5,0.5,−2.5), A_8: (1.5,−0.5, −0.5), B_1: (0.0,0.0,0.0), B_2: (1.5,1.5,−1.5), B_3: (1.0,1.0, −2.0), B_4: (1.0,0.0,0.0), B_5: (0.5,0.5,−1.5), B_6: (2.0,1.0, −2.0), B_7: (0.5,−0.5,−0.5), B_8: (2.0,0.0,−1.0).

3. SQS-14 $A_{0.571}B_{0.429}$

Description: It is not possible to find an actual *special* quasirandom structure for $x=3/7$ with 14 atoms per unit cell, since no such bcc-based structure satisfies $\Pi_p(\boldsymbol{\sigma})=1/49$ even for the first pair shell. Instead, we choose to approximate the random alloy limit on a local scale by minimizing the least-squares sum over $|\Pi_f(\boldsymbol{\sigma})-(1/7)^l|$ for a number of short-range correlation functions (first ten pair shells, and three- and four-body figures up to the third-nearest-neighbor maximum vertex distance). For $x=3/7$, the structure with 14 atoms/unit cell which satisfies this is a triclinic structure that can be described as an $A_4B_2A_2BABAB_2$ sequence (superlattice) of (831) atomic planes.

Space group: $P1$ (No. 1 in the International Tables for Crystallography[66]).

Primitive cell (Cartesian coordinates):

$a_1=(1.5,1.5,0.5)$, $a_2=(-0.5,1.5,0.5)$, $a_3=(-0.5, -0.5,2.5)$

Atomic coordinates (Cartesian coordinates):

A_1: (0.0,0.0,2.0), A_2: (0.0,1.0,2.0), A_3: (0.5,1.5,1.5), A_4: (0.0,1.0,3.0), A_5: (0.5,1.5,2.5), A_6: (0.5,0.5,0.5), A_7: (0.5,0.5,2.5), A_8: (−0.5,0.5,1.5), B_1: (0.0,0.0,0.0), B_2: (0.5,0.5,1.5), B_3: (1.0,1.0,1.0), B_4: (−0.5,0.5,2.5), B_5: (0.0,1.0,1.0), B_6: (0.0,0.0,1.0).

[1] W. Bragg and E. Williams, Proc. R. Soc. London **A145**, 699 (1934).

[2] R. Kikuchi, Phys. Rev. **81**, 988 (1951).

[3] C. Domb, in *Phase Transitions and Critical Phenomena*, edited by C. Domb and H. Green (Academic, London, 1974), Vol. 3, p. 358.

[4] K. Binder, Phys. Rev. Lett. **45**, 811 (1980).

[5] D. Styer, M. Phani, and J. Lebowitz, Phys. Rev. B **34**, 3361 (1986).

[6] F. Ducastelle, *Order and Phase Stability in Alloys* (North-

Holland, Amsterdam, 1991).

[7] J. Sanchez and D. de Fontaine, in *Structure and Bonding in Crystals*, edited by M. O'Keefe and A. Navrotsky (Academic, New York, 1981), Vol. 2, p. 117.

[8] J. Sanchez, F. Ducastelle, and D. Gratias, Physica A **128**, 334 (1984).

[9] A. Zunger, in *Statics and Dynamics of Alloy Phase Transformations*, edited by P. Turchi and A. Gonis (Plenum, New York, 1994), pp. 361–419.

[10] A. Zunger, L. Wang, G. Hart, and M. Sanati, Modell. Simul. Mater. Sci. Eng. **10**, 1 (2002).

[11] L. Ferreira, S.-H. Wei, and A. Zunger, Phys. Rev. B **40**, 3197 (1989).

[12] J. Connolly and A. Williams, Phys. Rev. B **27**, 5169 (1983).

[13] L. Ferreira, S.-H. Wei, and A. Zunger, Int. J. Supercomput. Appl. **5**, 34 (1991).

[14] Z. Lu, S.-H. Wei, A. Zunger, S. Frota-Pessoa, and L. Ferreira, Phys. Rev. B **44**, 512 (1991).

[15] Z. Lu, D. Laks, S.-H. Wei, and A. Zunger, Phys. Rev. B **50**, 6642 (1994).

[16] V. Ozoliņš, C. Wolverton, and A. Zunger, Phys. Rev. B **57**, 6427 (1998).

[17] C. Wolverton, V. Ozoliņš, and A. Zunger, Phys. Rev. B **57**, 4332 (1998).

[18] S. Müller, L.-W. Wang, A. Zunger, and C. Wolverton, Phys. Rev. B **60**, 16 448 (1999).

[19] M. Sanati, L. Wang, and A. Zunger, Phys. Rev. Lett. **90**, 045502 (2003).

[20] D. Laks, L. Ferreira, S. Froyen, and A. Zunger, Phys. Rev. B **46**, 12 587 (1992).

[21] M. Plutowski, *Survey: Cross-validation in Theory and Practice*, http://www.emotivate.com/CvSurvey.doc (1996).

[22] A. van de Walle and G. Ceder, J. Phase Equilib. **23**, 348 (2002).

[23] V. Blum and A. Zunger, Phys. Rev. B **69**, 020103 (2004).

[24] B. Predmore and R. Arsenault, Scr. Metall. **4**, 213 (1970).

[25] S. Singhal and W. Worrell, in *Proceedings of the International Symposium on Metallurgical Chemistry, Brunel University and National Physical Laboratory, UK, 1971*, edited by O. Kubaschewski (Her Majesty's Stationary Office, London, 1974), pp. 65–72.

[26] S. Singhal and W. Worrell, Metall. Trans. **4**, 1125 (1973).

[27] S. Singhal and W. Worrell, Metall. Trans. **4**, 895 (1973).

[28] C. Colinet, A. Bessoud, and A. Pasturel, J. Phys. F: Met. Phys. **18**, 903 (1988).

[29] C. Colinet and A. Pasturel, Physica B **159**, 275 (1989).

[30] C. Sigli and J. Sanchez, Acta Metall. **36**, 367 (1988).

[31] *Phase Equilibria, Crystallographic and Thermodynamic Data of Binary Alloys*, Vol. 5H of *Landolt-Börnstein, New Series, Group IV*, edited by B. Predel (Springer, Berlin, 1997).

[32] P. Turchi, A. Gonis, V. Drchal, and J. Kurdnovsky, Phys. Rev. B **64**, 085112 (2001).

[33] A. Carlsson, Phys. Rev. B **35**, 4858 (1987).

[34] A. Carlsson and J. Sanchez, Solid State Commun. **65**, 527 (1988).

[35] A. Carlsson, Phys. Rev. B **40**, 912 (1989).

[36] T. Mohri, K. Terakura, S. Tazikawa, and J. Sanchez, Acta Metall. Mater. **39**, 493 (1991).

[37] A. Pasturel, C. Colinet, A. Paxton, and M. van Schilfgaarde, J. Phys.: Condens. Matter **4**, 945 (1992).

[38] G. Rubin and A. Finel, J. Phys.: Condens. Matter **7**, 3139 (1995).

[39] G. Das, A. Arya, and S. Banerjee, Intermetallics **4**, 625 (1996).

[40] Y. Chen, T. Atago, and T. Mohri, J. Phys.: Condens. Matter **14**, 1903 (2002).

[41] C. Wolverton, V. Ozoliņš, and A. Zunger, J. Phys.: Condens. Matter **12**, 2749 (2000).

[42] J. E. Bernard, L. G. Ferreira, S.-H. Wei, and A. Zunger, Phys. Rev. B **38**, 6338 (1988).

[43] G. P. Srivastava, J. L. Martins, and A. Zunger, Phys. Rev. B **31**, 2561 (1985).

[44] A. Ruban, S. Simak, S. Shallcross, and H. Skriver, Phys. Rev. B **67**, 214302 (2003).

[45] Z. Lu, S.-H. Wei, and A. Zunger, Phys. Rev. B **45**, 10 314 (1992).

[46] S.-H. Wei, A. Mbaye, L. Ferreira, and A. Zunger, Phys. Rev. B **36**, 4163 (1987).

[47] J. Shao, J. Am. Stat. Assoc. **88**, 486 (1993).

[48] J. Ihm, A. Zunger, and M. Cohen, J. Phys. C **12**, 4409 (1979).

[49] G. Kresse and J. Furthmüller, Phys. Rev. B **54**, 11 169 (1996).

[50] G. Kresse and J. Furthmüller, Comput. Mater. Sci. **6**, 15 (1996).

[51] P. Blöchl, Phys. Rev. B **50**, 17 953 (1994).

[52] G. Kresse and A. Joubert, Phys. Rev. B **59**, 1758 (1999).

[53] J. Perdew and A. Zunger, Phys. Rev. B **23**, 5084 (1981).

[54] H. Monkhorst and J. Pack, Phys. Rev. B **13**, 5188 (1976).

[55] S. Froyen, Phys. Rev. B **39**, 3168 (1999).

[56] P. Blöchl, O. Jepsen, and O. Andersen, Phys. Rev. B **49**, 16 223 (1994).

[57] P. Blaha, K. Schwarz, and J. Luitz, WIEN97 (TU Wien, Vienna, 1999).

[58] D. Gaunt, Proc. Phys. Soc. London **92**, 150 (1967).

[59] D. Landau, Phys. Rev. B **16**, 4164 (1977).

[60] G. Geach and D. Summers-Smith, J. Inst. Met. **80**, 143 (1952).

[61] F. Guillemot, M. Boliveau, M. Bohn, J. Debuigne, and D. Ansel, Int. J. Refract. Met. Hard Mater. **19**, 183 (2001).

[62] A. Zunger, S.-H. Wei, L. Ferreira, and J. Bernhard, Phys. Rev. B **65**, 353 (1990).

[63] C. Sigli, M. Kosugi, and J. Sanchez, Phys. Rev. Lett. **57**, 253 (1986).

[64] Z. Bangwei and O. Yifang, Phys. Rev. B **48**, 3022 (1993).

[65] J. Perdew and Y. Wang, Phys. Rev. B **45**, 13 244 (1992).

[66] *International Tables for Crystallography*, Vol. A, edited by T. Hahn (D. Reidel, Dordrecht, 1983).

[67] *Pearson's Handbook of Crystallographic Data for Intermetallic Phases, 2nd ed.*, edited by P. Villars and L. Calvert (ASM International, Materials Park, OH, 1991).